

Multifunctional Nanoplatfoms as Cascade-Responsive Drug-Delivery Carriers for Effective Synergistic Chemo-Photodynamic Cancer Treatment

Fan Li

Shanghai 9th Peoples Hospital Affiliated to Shanghai Jiaotong University School of Medicine

Yan Liang

Qingdao University

Miaochen Wang

Shanghai 9th Peoples Hospital Affiliated to Shanghai Jiaotong University School of Medicine

Xing Xu

Shanghai 9th Peoples Hospital Affiliated to Shanghai Jiaotong University School of Medicine

Fen Zhao

Shanghai 9th Peoples Hospital Affiliated to Shanghai Jiaotong University School of Medicine

Xu Wang

Shanghai 9th Peoples Hospital Affiliated to Shanghai Jiaotong University School of Medicine

Yong Sun

Qingdao University

Wantao Chen (✉ chenwantao196323@sjtu.edu.cn)

Shanghai 9th Peoples Hospital Affiliated to Shanghai Jiaotong University School of Medicine

<https://orcid.org/0000-0002-9307-162X>

Research Article

Keywords: Multifunctional nanoplatfom, pH-responsive amphiphilic polymer, Nuclear targeting, Drug delivery, Synergistic anticancer therapy

Posted Date: March 15th, 2021

DOI: <https://doi.org/10.21203/rs.3.rs-286273/v1>

License:  This work is licensed under a Creative Commons Attribution 4.0 International License.

[Read Full License](#)

Abstract

Synergistic chemo-photodynamic therapy has attracted increasing attention in the field of cancer treatment. Herein, a pH cascade-responsive micellar nanoplatform with nucleus-targeted ability was fabricated, which could implement effective synergistic chemo-photodynamic cancer treatment. In this micellar nanoplatform, 5-(4-carboxyphenyl)-10,15,20-triphenylporphyrin (Por), a photodynamic therapy (PDT) agent, was utilized to carry the novel anticancer drug GNA002 to construct a hydrophobic core, and cyclic RGD peptide (cRGD)-modified polyethylene glycol (PEG) (cRGD-PEG) connected the cell-penetrating peptide hexaarginine (R_6) through a pH-responsive hydrazone bond (cRGD-PEG-N=CH- R_6) to serve as a hydrophilic shell for increasing blood circulation time. After passively accumulating in tumor sites, the self-assembled GNA002-loaded nanoparticles were actively internalized into cancer cells via cRGD ligands. Once phagocytosed by lysosomes, the acidity-triggered detachment of the cRGD-PEG shell led to the formation of R_6 -coated secondary nanoparticles and subsequent R_6 -mediated nucleus-targeted drug delivery. Combined with GNA002-induced nucleus-specific chemotherapy, reactive oxygen species produced by Por under 532-nm laser irradiation achieved a potent synergistic chemo-photodynamic cancer treatment. Moreover, our *in vitro* and *in vivo* anticancer investigations proved this ideal multifunctional nanoplatform showed a high cancer-suppression efficacy and could be a promising candidate for synergistic anticancer therapy.

Background

Although methods of early diagnosis and treatment of cancers have improved in recent years, the treatment of malignant tumors remains an arduous challenge since deep cancer cannot be completely removed by surgery, resulting in cancer recurrence and systemic metastasis [1–3]. Chemotherapy is presently the main cancer-treatment strategy [4–6], and potent traditional chemotherapeutic drugs such as doxorubicin as well as cisplatin and other novel anticancer drugs such as GNA002 exhibit profound anticancer efficacy [7, 8]. GNA002, a derivative of naturally-derived gambogic acid, has shown powerful cytotoxicity against various solid malignant tumors including lung and breast cancers. As we have previously demonstrated, GNA002 diffuses freely into the nuclei of cancer cells where it covalently binds to the Cys668 of the EZH2 field, triggering EZH2 degradation through the COOH terminus of the Hsp70-interacting protein (CHIP)-mediated ubiquitination, which relies on EZH2 to inhibit cancer growth [9]. Nevertheless, low bioavailability as well as poor water solubility of GNA002 and high toxicity of other chemotherapeutic drugs limit their applications in clinical medicine and long-term cancer therapy.

To overcome such limitations, photodynamic therapy (PDT) [10–12], a cancer treatment mode that can be spatiotemporally controlled, has shown good results in various minimally invasive cancer treatments. The basic principle of PDT cancer treatment is that the half-life of the photosensitizer given systematically or locally is different in cancerous and normal tissues [13]. Therefore, after a while, the photosensitizer concentration in cancerous tissues is remarkably higher than that in normal ones, thereby selectively retaining the photosensitizer in cancer cells. When the photosensitizer is subsequently activated by being subjected to excitation of a specific wavelength, cytotoxic reactive oxygen species

(ROS), especially singlet oxygen, are produced, leading to cancer cell necrosis and apoptosis [14, 15]. However, PDT cannot eliminate cancer cells owing to the limited laser penetration and hypoxia in tumor tissues, thus presenting insufficient curative effects [16–18].

Therefore, a combination of nanoparticle drug delivery systems (NDDSs) [19–24] balances the relationship between GNA002-mediated chemotherapy and PDT and enhances the efficacy of anticancer treatments. In detail, combining cancer therapy based NDDSs [25–27] can not only utilize the PDT advantage of selective cytotoxicity to cancer cells while minimizing the undesirable side effects to the surrounding normal cells, but also take advantage of chemotherapy to eliminate deep cancer cells and overcome the PDT shortcomings. Moreover, the ideal NDDSs should be specifically sensitive to target sites by responding to biological and environmental stimuli [28, 29], precisely delivering drugs from the injection sites to the intracellular targets where they become activated [30, 31], and controllably exercise their unique functions [32].

Consequently, a new type of multifunctional nanoplatform was developed based on a pH-responsive nucleus-targeted amphiphilic polymer for synergistic chemo-photodynamic cancer therapy. As shown in Scheme 1, hexaarginine (R_6) was linked between polyethylene glycol (PEG) and 5-(4-carboxyphenyl)-10,15,20-triphenylporphyrin (Por) by the amidation of the carboxyl and amino groups to form Por- R_6 and by the pH-responsive hydrazine bond between R_6 and PEG to yield PEG-N = CH- R_6 -Por. With the Michael addition of the cRGD to the PEG terminal group, the ultimate cRGD-PEG-N = CH- R_6 -Por (cPRP) triblock copolymer was fabricated. After the copolymer had self-assembled with chemotherapeutic drug GNA002, the GNA002-loaded nanoparticles (GNA002@cPRP) were injected subcutaneously into mice with cancer to carry out synergistic chemo-photodynamic therapy. First, the nanosized GNA002@cPRP passively accumulated in tumors via the EPR effect. The cRGD-PEG shell protected the drug-loaded nanoparticles from reticuloendothelial system clearance, prolonged the blood circulation time, and promoted active cancer cell targeting. Once the GNA002@cPRP nanoparticles were endocytosed by cancer cells and subsequently exposed to the acidic lysosome environment, the acidity-triggered detachment of the cRGD-PEG shell led to the formation of R_6 -coated secondary nanoparticles. Then, the positively charged R_6 -coated secondary nanoparticles facilitated lysosomal escape. Nucleus-targeted GNA002 accumulation, as well as nucleus-specific cytotoxic effects, followed. Finally, cytotoxic ROS produced by Por-mediated PDT under 532-nm laser irradiation were also able to induce the death of cancer cells which as a result, improved the anticancer treatment. Hence, our study integrates pH-responsive nucleus-targeted GNA002 chemotherapy and Por-mediated PDT, thus providing a promising multifunctional nanoplatform with applications in synergistic anticancer therapy.

Methods

Reagents, Cell Lines, and Animals

5-(4-Carboxyphenyl)-10,15,2-triphenylporphyrin (Por) and Boc-Mal were obtained from Zhengzhou Alfa Chemical Co., Ltd. (Zhengzhou, China). GL Biochem Ltd. (Shanghai, China) was the source of Cyclic (RGDyC), KR₆C (KRRRRRRC) and O-benzotriazole-N, N, N', N'-tetramethyluronium hexafluorophosphate (HATU). Mal-PEG-Hz (Mw = 2000 g/mol) was purchased from HUATENG PHARMA (Changsha, China). 5-formyl-2,4-dimethyl-1H-pyrrole-3-carboxylic acid was obtained from TCI Chemical Industry Development Co., Ltd. (Shanghai, China). mPEG-CH = N-PCL (mP) was procured from Xi'an ruixi Biological Technology Co., Ltd. (Xi'an, China). N, N-diisopropylethylamine (DIPEA) and Trifluoroacetic acid (TFA) were purchased from Adamas Reagent, Ltd. (Shanghai, China). Anhydrous methyl alcohol and N, N-dimethylformamide (DMF) was procured from Shanghai Aladdin Biochemical Technology Co., Ltd. (Shanghai, China). Fetal bovine serum (FBS) and Dulbecco's modified Eagle's medium (DMEM) were procured from Gibco Life Technologies (California, USA). Dalian Meilun Biotechnology Co., Ltd. (Dalian, China) was the source of DiD perchlorate, Hoechst 33342, 2',7'-dichlorodihydrofluorescein diacetate (DCFH-DA), cell counting kit-8 (CCK-8), LysoTracker Green DNA-26 and Annexin V-FITC/PI.

Mouse embryo fibroblast cells (NIH-3T3), human cervical carcinoma cells (HeLa), human tongue cancer cells (HN6), human malignant melanoma cells (A375), human breast cancer cells (MCF-7), and human pharynx cancer cells (HN30) were provided by the Cell Bank of the Chinese Academy of Sciences (Shanghai, China).

Male and female BALB/c nude mice (17–20 g) were provided by the Shanghai Laboratory Animal Center (Shanghai, China).

Characterization of cPRP

The ultraviolet-visible (UV-vis) spectra of cRGD, PEG, and cRGD-PEG were recorded on a UV-3101PC spectroscope (Shimadzu, Japan). Electrospray-ionization mass spectrometry (LCQ Orbitrap XL, USA) was used to characterize the molecular weights of Por-R₆-CHO and its intermediate products. The gel permeation chromatography (GPC, Agilent 1200 Series, USA) with tetrahydrofuran as mobile phase was applied to determine the outflow time of cRGD-PEG, cPRP and cPRP at pH 5.0. The cPRP ¹H nuclear magnetic resonance (NMR) spectra were generated under different pH conditions using a Bruker DRX 600 MHz NMR spectrometer (USA) and hexadeuterated dimethyl sulfoxide (DMSO-d₆). Transmission electron microscopy (TEM, Thermo Scientific Talos L120C, USA) was used to evaluate the morphology of the GNA002-loaded nanoparticles. The diameter, zeta potential, and PDI of the cPRP nanoparticles were measured by dynamic light scattering (DLS, Zetasizer Nano ZS, UK). High-performance liquid chromatography (HPLC, AB Sciex Quadrupole 5500, USA) was performed using a C18 4.6 × 250-mm column to determine the GNA002 concentration in the GNA002@cPRP nanoparticles.

Synthesis of cRGD-PEG-Hz

First, Mal-PEG-Hz (0.400 g, 0.2 mmol) and cRGD peptide (0.149 g, 0.25 mmol) were dissolved in 15 mL of deionized (DI) water, and the mixture was stirred at 25°C for 8 h under the protection of nitrogen to

complete the Michael addition. Then, the cRGD-PEG-Hz was purified by dialysis [molecular weight cutoff (MWCO) 1,000 Da] for 2 days to remove any residual cRGD and was obtained by lyophilization.

Synthesis of Por-R₆-Boc

First, KR₆C (0.119 g, 0.1 mmol) and Boc-Mal (0.072 g, 0.3 mmol) were fully dissolved in 8 mL of anhydrous dimethylformamide (DMF), and KR₆Boc was formed after stirring the mixture at 25°C for 8 h under the protection of nitrogen. Then, HATU (0.076 g, 0.2 mmol), Por (0.132 g, 0.2 mmol) and DIPEA (0.070 mL, 0.4 mmol) were fully dissolved in 10 mL of anhydrous DMF, and the mixture was stirred at 25°C for 0.5 h to activate the Por carboxyl group. Next, the KR₆Boc solution was added dropwise to the activated Por solution, and the mixture was stirred at 25°C for 0.5 h under the protection of nitrogen to complete the amidation. Subsequently, the product was transferred to a dialysis tube (MWCO 1,000 Da) and was dialyzed against DMF solution for 1 day and then against DI water for 1 day to remove any residual Por and Boc-Mal. Finally, the Por-R₆-Boc was obtained by lyophilization.

Synthesis of Por-R₆-NH₂

Briefly, the Boc groups of the as-synthesized Por-R₆-Boc were removed by mixing the Por-R₆-Boc with 5 mL of trifluoroacetic acid (TFA) in 5 mL of dichloromethane and stirring at 30°C for 2 h. Then, pure Por-R₆-NH₂ was obtained after rotary evaporation at 30°C and subsequent precipitation in cold anhydrous diethyl ether.

Synthesis of Por-R₆-CHO

First, HATU (0.114 g, 0.3 mmol), 5-formyl-2,4-dimethyl-1H-pyrrole-3-carboxylic acid (0.050 g, 0.3 mmol), and DIPEA (0.104 mL, 0.6 mmol) were fully dissolved in 10 mL of anhydrous DMF and stirred at 25°C for 0.5 h to activate the carboxyl group on the 5-formyl-2,4-dimethyl-1H-pyrrole-3-carboxylic acid. Then, the as-synthesized Por-R₆-NH₂ (0.261 g, 0.1 mmol) was dissolved in 10 mL of anhydrous DMF and added dropwise to the activated 5-formyl-2,4-dimethyl-1H-pyrrole-3-carboxylic acid solution. The amidation was completed after stirring at 25°C for 0.5 h under the protection of nitrogen. Finally, the pure Por-R₆-CHO was obtained via dialysis (MWCO 1,000 Da) against DMF solution and DI water for 2 days and subsequent lyophilization.

Synthesis of cPRP

The as-synthesized Por-R₆-CHO (0.221 g, 0.08 mmol) and cRGD-PEG-Hz (0.309 g, 0.12 mmol) were added to 20 mL of anhydrous methanol with acetic acid as an acid catalyst and stirred at 28°C for 2 days under nitrogen. Then, the purified cPRP was dialyzed (MWCO 3,000 Da) for 2 days and then lyophilized.

Preparation of Blank, GNA002-, and DiD-loaded nanoparticles

Preparation of the blank cPRP nanoparticles: First, 8 mg cPRP powder was dissolved in 1 mL DMF. Then the solution was added dropwise to 15 mL DI water stirring for 24 h. Finally, the stirred solution was dialyzed (MWCO 3000 Da) against DI water to obtain the blank nanoparticle solution.

Preparation of the drug-loaded cPRP nanoparticles (drug including GNA002 and DiD): First, 2 mg of drug and 8 mg of cPRP were ultrasonicated in 1 mL DMF until fully dissolved. The remaining steps were the same as the blank nanoparticles. For fluorescence labeling, DiD perchlorate was used as the model drug owing to the lack of fluorescence of GNA002. The DiD-loaded cPRP and mPEG-CH = N-PCL (mP) nanoparticles were prepared using similar approaches to those used to prepare the drug-loaded cPRP ones.

Drug-Loading Capacity and Encapsulation Efficiency of GNA002@cPRP

The concentration of GNA002 encapsulated in the cPRP nanoparticles was measured by HPLC in methanol and was compared against the standard concentration curve obtained from free GNA002. The HPLC C18 column was maintained at 30°C; the mobile phase consisted of a mixture of methanol and water (90:10, v/v) flowing at 1.0 mL/min; and 10 μ L of the GNA002/methanol solutions were injected into the column. The HPLC detection wavelength was 360 nm. The drug-loading capacity (DLC) and encapsulation efficiency (EE) were calculated using the following formulas:

$$\text{DLC (\%)} = (\text{weight of loaded GNA002}) / (\text{total weight of loaded GNA002 and nanoparticles}) \times 100\% \quad (1)$$

$$\text{EE (\%)} = (\text{weight of loaded GNA002}) / (\text{weight of feeding GNA002}) \times 100\% \quad (2)$$

In Vitro Drug Release

Briefly, the GNA002-release profiles of the GNA002@cPRP nanoparticles were measured *in vitro* under sink conditions. First, 2 mL of GNA002@cPRP nanoparticle solution was placed into two dialysis bags (MWCO = 3,000), immersed in 20 mL of PBS at pH 7.4 and 5.0 with 0.1% Tween 80, and constantly shaken at 37°C. At different points in time, 1 mL of the externally released buffer was collected and prepared to measure the GNA002 concentration by HPLC. Meanwhile, 1 mL of fresh PBS was added to replenish the volume for further study.

In Vitro Cellular Uptake

The *in vitro* cellular uptake was investigated using confocal-laser scanning microscopy (CLSM), flow cytometry, and HeLa cancer cells. For the CLSM investigation, HeLa cells with 4×10^5 cells per well were seeded into glass plates (35 mm). The cells were cultured overnight, and DiD@cPRP nanoparticles (DiD: 10 μ g/mL) were then added to four of the glass plates, two of which had been pretreated with free cRGD for 2 h to fill the $\alpha_v\beta_3$ receptor. The cells were then incubated for 1 h or 3 h, respectively, and the medium was removed. The HeLa cells were washed thrice with PBS and fixed with 4% paraformaldehyde for 15 min, and the cell nuclei were dyed for 5 min with Hoechst 33342 stain ($E_m = 460$ nm; $E_x = 346$ nm), which

was also used for the following *in vitro* lysosomal escape and nucleus distribution studies. The images of the HeLa cells were captured using CLSM after the cells had been washed thrice with precooled PBS.

For the flow cytometry measurements, HeLa cells with 1.5×10^6 cells per well were seeded into 6-well plates. The cells were cultured overnight with the same $\alpha_v\beta_3$ -receptor pretreatment. DiD@cPRP nanoparticles were then added to the plates, and the cells were incubated for 1 h or 3 h, respectively. Subsequently, the HeLa cells were washed thrice with PBS, harvested with trypsin, and conducted on a BD FACSCalibur flow cytometer (Becton Dickinson, USA) (DiD: $E_m = 663$ nm; $E_x = 644$ nm).

In Vitro **Lysosomal Escape**

HeLa cells with 4×10^5 cells per well were seeded into glass plates. The cells were cultured overnight, and then free-DiD or DiD@cPRP nanoparticles (DiD: 10 μ g/mL) were added to two of the glass plates, and the cells were then incubated for 2 h or 4 h, respectively. The medium was then removed, and the same protocol used for the cellular uptake was followed. Meanwhile, the HeLa cells were stained with LysoTracker Green ($E_m = 511$ nm; $E_x = 504$ nm) for 0.5 h, washed thrice with precooled PBS, and visualized by CLSM.

In Vitro **Nuclei Distribution**

DiD-loaded mP nanoparticles were used as the negative control group for the *in vitro* nucleus distribution analysis.

HeLa cells with 4×10^5 cells per well were seeded into glass plates (35 mm). The cells were cultured overnight, and then DiD@mP or DiD@cPRP nanoparticles (DiD: 10 μ g/mL) were added to two of the glass plates, and the cells were incubated for 4 h or 8 h, respectively. The medium was then removed, and the same protocol used for cellular uptake was followed. Simultaneously, the HeLa cells were washed thrice with PBS and monitored using CLSM. The images were processed and analyzed using ImageJ software.

In Vitro **Drug Penetration**

HeLa multicellular cancer spheroids (MCSs) were established to examine the *in vitro* drug penetrability. First, 50 μ L of 1% hot agarose gel was added to 96-well plates and cooled under a UV lamp for 30 min. Then, HeLa cells (6×10^3) were carefully seeded into the precoated plate and incubated for 5 days. On reaching the diameter of 100–150 μ m, the MCSs were transferred to glass dishes (35 mm) and treated with DiD@mP and DiD@cPRP nanoparticles for 4 h. At last, the MCSs were collected, rinsed with PBS twice, and monitored using CLSM. The images were processed and analyzed using ImageJ software.

In Vitro **ROS measurements**

HeLa cells with 4×10^5 cells per well were seeded into glass plates (35 mm). The cells were cultured overnight, and then culture medium, GNA002, cPRP nanoparticles and GNA002@cPRP nanoparticles were added to two of the glass plates, and the cells were incubated for 4 h, respectively. After incubation

of 4 h, the cells were irradiated by a laser ($\lambda_{\text{ex}} = 532 \text{ nm}$; 100 mW; 10 min per plate) and stained with DCFH-DA for 20 min. Subsequently, the HeLa cells were rinsed thrice with precooled PBS and observed using CLSM.

Assessment of cPRP-Nanoparticle and Laser Irradiation Cytotoxicity

In order to avoid the selective effects of cPRP nanoparticles on certain cells, we used normal NIH 3T3 cells and a variety of cancer cells to verify the biosafety of blank cPRP nanoparticles and laser irradiation.

The cytotoxicity of blank cPRP nanoparticles and laser irradiation against NIH 3T3, HeLa, HN6, A375, MCF-7, and HN30 cancer cells were assessed using a CCK-8 assay. First, each type of cell (3×10^3) was seeded into 96-well plates. The cells were cultured overnight; the original medium was removed and replaced with medium (100 μL) including different concentrations of cPRP nanoparticles; and the nanoparticle-free cells were irradiated with a laser ($\lambda_{\text{ex}} = 532 \text{ nm}$; 100 mW; 10 min per well) after 4 h of incubation. Then, the medium was replaced with the prepared CCK-8 solution after the cells had been incubated for another 48 h. Finally, the absorbance was recorded at 450 nm for evaluation.

In Vitro Anticancer Efficacy

Similarly, we used HeLa, HN6, A375, MCF-7, and HN30 cancer cells to avoid the selective effects of cPRP nanoparticles on certain cancer cells and to verify its potent anticancer efficacy *in vitro*.

Briefly, HeLa, HN6, A375, MCF-7, and HN30 cancer cells with 3×10^3 cells per well were seeded into 96-well plates. The cells were cultured overnight, and the original medium was removed and then replaced with medium (100 μL) including different concentrations of GNA002, GNA002@cPRP nanoparticles with or without laser irradiation ($\lambda_{\text{ex}} = 532 \text{ nm}$; 100 mW; 10 min per well) and cisplatin. The cancer cells were incubated for another 48 h and then examined using a CCK-8 assay.

To further study cell apoptosis, HeLa, HN6, A375, MCF-7, and HN30 cancer cells with 1.5×10^5 cells per well were seeded into 6-well plates. The cells were cultured overnight and then GNA002, GNA002@cPRP nanoparticles with or without laser irradiation and cisplatin were added to the wells to replace the original medium. The cancer cells were incubated for another 48 h and were then washed twice with binding buffer, harvested with trypsin, stained with PI as well as Annexin V-FITC for 20 min, and measured by flow cytometry.

In Vivo Fluorescence Imaging

For the *in vivo* and *ex vivo* biodistribution studies of the GNA002@cPRP nanoparticles in the tumor tissues, HeLa cells were implanted subcutaneously into the right flank of BALB/c female mice to establish the HeLa cancer models. When the tumor volume reached 50–100 mm^3 , the free-DiD and

DiD@cPRP (DiD concentration: 0.5 mg/kg) nanoparticles were injected via tail vein. *In vivo* fluorescence imaging was conducted by an IVIS[®] Imaging System (PerkinElmer, USA) at prescribed time. Subsequently, major organs and tumors were imaged *ex vivo* after sacrificing the mice.

In Vivo Anticancer Efficacy

To evaluate the *in vivo* anticancer efficacy, HeLa tumor-bearing mice were established as a cancer model, as described in Sect. 2.17. Moreover, HN6 tumor-bearing mice were also established as another cancer model to avoid the selective effects of cPRP nanoparticles. When the tumor volume reached 50–100 mm³, the mice were randomly categorized into six groups (n = 6) and were treated with saline, saline plus laser irradiation ($\lambda_{\text{ex}} = 532$ nm; 100 mW; 10 min at 24 h post-injection), GNA002, cisplatin, GNA002@cPRP nanoparticles, or GNA002@cPRP nanoparticles plus laser irradiation at 3-day intervals by venous injection into the tail with the dosage of 3 mg/kg. The body weights and tumor volumes were detected every other day. The tumor volumes were calculated using the formula: $V = \frac{1}{2} l \times w^2$, where V , l , and w are volume (in mm³), length, and width, respectively. On day 14, all mice were sacrificed, and their major organs and tumor tissues were gathered and fixed with 4% formaldehyde. The tumor tissues were stained with hematoxylin and eosin (H&E) for histological assessment, and TUNEL as well as Ki-67 assays were performed to analyze the cancer cell proliferation and apoptosis.

Statistical Analysis

Data are shown as mean \pm standard deviation. Statistical significance was estimated by Student's unpaired *t*-test and two-way ANOVA, and different statistical significance were set at * $P < 0.05$, ** $P < 0.01$, *** $P < 0.001$, and **** $P < 0.0001$, respectively.

Results And Discussion

Construction and Characterization of cPRP

The aim of this study was to fabricate pH-responsive nucleus-targeted nanoparticles for enhanced synergistic chemo-photodynamic therapy. The synthesis of amphiphilic cPRP as a drug carrier, is presented in Supplementary Scheme 1. Mass spectrum, UV-vis, GPC, and ¹H NMR results confirmed the synthesis of different intermediate products and validated that the cPRP chemical structure was correct. First, the mass spectrum results for Por-R₆-Boc (m/z [M + 3H]³⁺: 903.10840; [M + 4H]⁴⁺: 677.58392; [M + 5H]⁵⁺: 542.26868), Por-R₆-NH₂ (m/z [M + 3H]³⁺: 869.75958; [M + 4H]⁴⁺: 652.57135; [M + 5H]⁵⁺: 522.25818), and Por-R₆-CHO (m/z [M + 3H]³⁺: 919.44159; [M + 4H]⁴⁺: 689.83350; [M + 5H]⁵⁺: 552.26801) verified that the molecular weights were correct (Fig. 1a-c). Then, the UV-vis spectrum of cRGD-PEG-Hz showed the characteristic absorption band of cRGD at 275 nm, proving the grafting of the cRGD peptide (Fig. 1d). Finally, the GPC result showed only one peak in the cPRP spectra in Fig. 1e, indicating the absence of any residual Por-R₆-CHO, and the outflow time of both compounds verified the cPRP

synthesis. In addition, the cPRP characteristic peaks are clearly marked in the ^1H NMR spectra (Fig. 1f), which is consistent with the GPC results.

Physicochemical Properties and pH-Responsiveness of cPRP and GNA002@cPRP Nanoparticles

The cPRP and GNA002-loaded cPRP amphiphiles self-assembled into nanoparticles when they were transferred from the DMF to the DI water. With GNA002 loaded into the nanoparticles by hydrophobic interactions, an encapsulating efficiency of $71.49 \pm 1.21\%$ and a higher drug-loading capacity of $14.29 \pm 0.24\%$ were achieved. In addition, the TEM images of the cPRP and GNA002@cPRP nanoparticles showed uniformly spherical morphologies, and the corresponding zeta potentials and mean diameters were -6.51 ± 0.58 mV and -6.23 ± 0.11 mV and 126.30 ± 0.62 nm and 156.67 ± 0.47 nm with a low PDI (< 0.2), respectively, as detected by DLS (Fig. 2a, 2b, and 2d). The larger mean diameter of the GNA002@cPRP nanoparticles was probably due to the encapsulation of the GNA002 in the center of the cPRP nanoparticles. Importantly, the negatively charged surface of the cPRP and GNA002@cPRP nanoparticles helped avoid the adsorption of plasma proteins *in vivo*, thereby prolonging the systemic circulation time [33].

To evaluate the stability and pH-responsiveness of the drug-loaded cPRP nanoparticles, the changes in nanoparticle size were measured in different media with DLS. Compared with the slight changes in size observed in the medium containing serum and PBS at pH 7.4, the size gradually increased within 12 h and decreased sharply between 12–24 h in PBS at pH 5.0 (Fig. 2e). The results indicated that the GNA002@cPRP nanoparticles exhibited satisfactory stability during cell incubation and blood circulation. It also showed that when the nanoparticles had been phagocytosed by lysosomes, the pH-responsive hydrazone bond between the PEG and R_6 was cleaved, resulting in smaller sized R_6 -coated secondary nanoparticles (GNA002@RP). In addition, the cPRP GPC spectra at pH 5.0, as well as the cPRP ^1H NMR spectra generated at pH 7.4 and 5.0, both validated the hydrazine bond of cPRP could be cleaved in acidic environment (Fig. S1a-b). The zeta potentials, mean diameters, and PDIs of the GNA002@RP nanoparticles were 11.83 ± 0.23 mV, 102.17 ± 0.67 nm, and 0.27 ± 0.01 , respectively.

The TEM image shows that the GNA002@RP nanoparticles were uniformly spherical, which is in accord with the DLS results (Fig.

2c-d). Furthermore, the positively charged surface of the GNA002@RP nanoparticles had promoted lysosomal escape.

In Vitro Drug Release

To further investigate the pH-responsive behaviors of the GNA002@cPRP nanoparticles, the GNA002 release profiles were measured in PBS at pH 7.4 and 5.0 under sink conditions (Fig. 2f). Only approximately 10% of the GNA002 had leaked from the GNA002@cPRP nanoparticles at pH 7.4, presenting the superior stability of GNA002-loaded cPRP nanoparticles in the blood. However, at pH 5.0

(imitating an acidic tumor intracellular environment), approximately 70% of the GNA002 was released from the GNA002@cPRP nanoparticles at 48 h, suggesting excellent pH-responsiveness of the GNA002@cPRP nanoparticles to the tumor microenvironment. Moreover, the release curve generated at pH 5.0 presented an early rapid-burst release followed by continuous release. Specifically, less than 15% of drug GNA002 was leaked in the first 2 h, and up to 60% was released 10 h later. The results suggest that the slow release in the first 2 h could ensure the GNA002@cPRP stability in the blood circulation and cancer cell cytoplasm, causing a slight loss before reaching the nuclei, and that the fast release during the next 10 h could improve GNA002 utilization after reaching the cancer-cell nuclei.

In Vitro Cellular Uptake

To evaluate the cellular uptake efficiency of the cPRP nanoparticles, HeLa cancer cells and DiD were used as the model cells and model drugs, respectively, and were monitored by CLSM and flow cytometry. As shown in Fig. 3a, the HeLa cells treated with the DiD@cPRP nanoparticles presented clearly accumulated weak to strong red fluorescence from 1 h to 3 h, while the free-cRGD pretreatment group barely showed any accumulated red fluorescence, indicating that blocking the integrin $\alpha_v\beta_3$ receptor had reduced the cellular uptake of the DiD@cPRP nanoparticles.

In addition, the cellular uptake of the DiD@cPRP nanoparticles was quantitatively investigated by flow cytometry (Fig. 3b). The mean fluorescence intensity (MFI) of the DiD increased from 1 h to 3 h, indicating that the nanoparticle endocytosis was time-dependent and that the nanoparticles continued to ingest over time. In addition, the MFI of the DiD@cPRP nanoparticles pretreated with cRGD was measured as $12,043.67 \pm 132.79$ and $19,800.67 \pm 355.53$ at 1 h and 3 h, respectively, both of which were significantly lower than those of the cRGD-unsaturated receptor group, thereby demonstrating that the $\alpha_v\beta_3$ -receptor-mediated endocytosis had efficiently facilitated the cellular uptake of the DiD@cPRP nanoparticles, which is consistent with the CLSM results. Taken together, the results suggest that cRGD-mediated active targeting is a crucial factor for the uptake of DiD@cPRP nanoparticles, thereby promoting their dispersion into the cancer-cell nuclei.

In Vitro Lysosomal Escape

To investigate the intracellular distribution of the DiD@cPRP nanoparticles after the cellular uptake by endocytosis, the DiD as the model drug with red fluorescence and the lysosomes of the HeLa cells labeled with LysoTracker Green were observed by CLSM after 2 h and 4 h incubation. As illustrated in Fig. 3c, the cells incubated with free DiD for 2 h or 4 h showed yellow fluorescence (originating from the colocalization of red and green fluorescence) in the HeLa-cell cytoplasm, suggesting that most of the DiD had been devoured by the lysosomes. As for the DiD@cPRP nanoparticles, nearly all of the DiD@cPRP red fluorescence was overlaid with the lysosome green fluorescence after 2 h incubation, indicating the colocalization of the DiD and the lysosome. However, only tiny amounts of overlapping yellow fluorescence remained at 4 h, and most of the red and green fluorescence existed independently, thereby verifying that the acidic lysosome environment had triggered the cleavage of the cPRP hydrazone bond

and that numerous guanidine-group positive charges on the secondary-nanoparticle surfaces had facilitated lysosomal escape by the “proton sponge” effect.

In Vitro Nuclei Distribution

To investigate the R₆ peptide-mediated nucleus-targetability of cPRP nanoparticles toward cancer cells, Hoechst 33342-labeled HeLa cells and DiD red fluorescence were monitored by CLSM (Fig. 4a). After the cells had been incubated with DiD@mP nanoparticles for 4 h or 8 h, few regions of purple fluorescence (originating from the colocalization of red and blue fluorescence) appeared in the HeLa-cell nuclei, suggesting that scanty DiD@mP nanoparticles were internalized within the nuclei. In contrast, several regions of purple fluorescence appeared in the HeLa-cell nuclei in the DiD@cPRP group, especially at 8 h, when the MFI of the DiD@cPRP was approximately double that of the DiD@mP. These results suggest that the R₆-mediated nucleus targeting had caused more DiD to enter the nuclei, thereby improving the efficiency of drug delivery.

In Vitro Drug Penetration

HeLa MCSs were used as the three-dimensional (3D) cancer models to assess the drug penetrability of the DiD@cPRP nanoparticles (Fig. 4b). After the HeLa MCSs had been incubated with DiD@mP or DiD@cPRP nanoparticles for 4 h, the MCSs in the DiD@cPRP group showed significantly higher red fluorescence than those in the DiD@mP group in the range of 20–60 μm in the central field, thereby proving that the cPRP nanoparticles had improved the drug penetrability.

In Vitro ROS Measurements

To verify the ROS generation of cPRP nanoparticles, HeLa cells stained with fluorescent probe DCFH-DA were detected by CLSM. The level of ROS production in HeLa cells was proportional to the intensity of DCFH-DA green fluorescence. As shown in Figure S1c, less green fluorescence was observed in controlled group and GNA002 group with or without laser irradiation, indicating hardly any ROS production in culture medium and GNA002. As expected, HeLa cells treated with laser-irradiated cPRP and GNA002@cPRP nanoparticles exhibited strong green fluorescence, thus validating that cPRP nanoparticles could produce a high level of ROS and implement effective PDT under 532 nm laser irradiation.

In Vitro Anticancer Efficacy

The cytotoxicity of the laser irradiation and the blank cPRP nanoparticles was examined using CCK-8 assays. As shown in Fig. 5a, the viabilities of the six-cell types remained above 90% after the cells had been treated either with blank cPRP nanoparticles at concentrations in the range of 0.781–100 μg/mL or had been irradiated for 10 min with a 532 nm wavelength laser, thereby proving that neither the blank cPRP nanoparticles nor the laser irradiation showed any appreciable cytotoxicity against both normal and cancerous cells. Moreover, the same cancer-cell lines were used to evaluate the anticancer efficacy of the GNA002-loaded cPRP nanoparticles *in vitro*, and cisplatin was used as a positive control against

GNA002. Figure 5b-f shows that the GNA002@cPRP nanoparticles in the 10 min laser-irradiation group presented the strongest anticancer efficacy compared with the groups of the free-GNA002, GNA002@cPRP nanoparticles without laser irradiation, and cisplatin. Furthermore, the IC₅₀ of the free-GNA002, GNA002@cPRP nanoparticles without laser irradiation, and cisplatin groups were significantly higher than that of the GNA002@cPRP laser-irradiated group for all the cancer-cell types, indicating that the synergistic efficiency of the GNA002 and Por-mediated PDT resulted in the most satisfactory cancer inhibitory effect, which was much better than those of the other groups.

The potency of the free-GNA002, GNA002@cPRP nanoparticles with or without laser irradiation, and cisplatin to induce cell apoptosis was assessed using Annexin V-FITC/PI assays for all the cancer-cell lines. As Fig. 6 shows, the apoptosis rates of the laser-irradiated GNA002@cPRP-nanoparticle group for all the cancer cells were higher than those of the other groups, and the results were consistent with those of the anticancer efficacy tests conducted using CCK-8 assays, thereby demonstrating that the best apoptosis was achieved by synergistically applying GNA002 and PDT.

In Vivo **Biodistribution**

The biodistribution of the drug-loaded cPRP nanoparticles was measured *in vivo* in HeLa mice with cancer. As shown in Fig. 7a, the DiD@cPRP-nanoparticle group presented much stronger red fluorescence intensity overall than the DiD group, and the red fluorescence intensity of the former peaked at 24 h. In contrast, red fluorescence did not accumulate at the tumor site in the latter at any predetermined time, and the real-time quantitative analysis of the red fluorescence intensity at the tumor sites in both groups reconfirmed these results (Fig. 7b). Moreover, *ex vivo* fluorescence imaging and quantitative analysis of the major organs and tumors, respectively were performed after 24 h tail vein injection (Fig. 7c-d). The average radiant efficiency of the free-DiD group at tumor sites was significantly lower than that of the DiD@cPRP group. Taken together, these results verified the superior accumulative tumor-targeting properties and prolonged tumor-retainability of the cPRP nanoparticles.

In Vivo **Anticancer Efficacy**

The HeLa and HN6 mouse models with cancer were used to assess the anticancer efficacy of the GNA002@cPRP nanoparticles. As illustrated in Fig. 8a and 8e, the tumors treated with either only saline or saline plus laser irradiation presented a rapid increase in tumor volumes within 14 days in both cancer-bearing mouse models, suggesting that the anticancer therapies of only saline and saline plus laser irradiation were ineffective. In addition, the groups receiving the free GNA002 exhibited minimal tumor suppression, with the HeLa and HN6 cancer-bearing mouse models showing tumor inhibition ratios (TIRs) of 43.7% and 34.8%, respectively (Fig. 8c and 8g). In contrast, although the groups treated with cisplatin presented better anticancer efficacy, the mice in those groups showed sharply decreased body weights after the second administration, compared with their counterparts of the laser-irradiated GNA002@cPRP-nanoparticle group by days 10 and 12 in the HeLa and HN6 cancer-bearing mouse models, respectively, thereby demonstrating the considerable side effects and systemic toxicity of

cisplatin (Fig. 8b and 8f). As for the other two groups, namely, the GNA002@cPRP nanoparticles with or without laser irradiation, the tumor growth was satisfactorily inhibited, especially in the laser-irradiated GNA002@cPRP group. Remarkable TIRs of 93.6% and 84.8% were achieved in the HeLa and HN6 cancer-bearing mouse models, respectively, with very little body-weight loss, thereby demonstrating the strongest tumor inhibitory efficacy and good biosafety. Furthermore, the tumor weights of all the groups were measured after the mice were sacrificed on day 14, and the results of which were agreed well with the above tumor volume results. Notably, the laser-irradiated GNA002@cPRP-nanoparticle group's tumor weight was just 6.3% and 6.7% of that of the saline group of the HeLa and HN6 cancer-bearing mouse models, respectively (Fig. 8d and 8h). Taken together, these results suggest that the synergistic chemo-photodynamic therapy contributed to the pronounced anticancer efficacy *in vivo*.

Histological and immunohistochemical methods including H&E, Ki-67, and TUNEL staining were performed to further assess the *in vivo* anticancer efficacy of the GNA002@cPRP nanoparticles. As illustrated in Fig. 9a, cancer-cell necrosis and apoptosis caused by the laser-irradiated GNA002@cPRP-nanoparticles were widely observed in the H&E-staining images. In addition, among all the groups, the laser-irradiated GNA002@cPRP nanoparticles showed the highest TUNEL expression in the TUNEL-staining images and the lowest cancer-cell proliferation in the Ki-67 staining images, thereby validating the outstanding potency of the anticancer efficacy induced by the synergistic GNA002@cPRP chemo-photodynamic therapy.

To evaluate the *in vivo* biosafety of the GNA002@cPRP nanoparticles, the major organs of all six groups of mice were analyzed by H&E staining. As shown in Fig. 9b, except for the massive hemorrhage in the lung and liver as well as scattered bleeding spots in the spleen of the cisplatin group, all the other groups showed no considerable histological damage to hearts, livers, spleens, lungs and kidneys, validating low toxicity of the GNA002@cPRP nanoparticles *in vivo*.

Conclusions

In this study, we successfully fabricated a pH cascade-responsive nucleus-targeted micellar nanoplatform to carry out GNA002 chemotherapy combined with Por-mediated PDT for enhanced anticancer therapy. The *in vitro* investigations confirmed that the cPRP nanoplatform could achieve satisfactory cellular uptake efficiency and nucleus-targeted GNA002 delivery. Moreover, the *in vivo* studies further demonstrated the biocompatible cPRP nanoplatform's superior tumor-targeting properties and prolonged tumor-retainability. Given its synergistic chemo-photodynamic therapeutic strategy, the GNA002-loaded cPRP nanoplatform comprehensively exhibited effective cytotoxicity against HeLa, HN6, A375, MCF-7, and HN30 cancer cells *in vitro* as well as HeLa and HN6 *in vivo*. Taken together, this study presents an ideal candidate for the development of multifunctional nanoplatforms in the field of synergistic anticancer therapy.

Declarations

Ethics approval and consent to participate

All animal experiments were conducted in line with the Ethical Committee of Shanghai Ninth People's Hospital, which is in line with the American Association for Laboratory Animal Science (AAALAS) guidelines.

Consent for publication

Not applicable.

Availability of data and materials

All data generated or analyzed during this research are included in this article.

Competing interests

The authors declare that they have no competing interests.

Funding

This study is supported by the National Program on Key Research Project of China (2016YFC0902700) and Shanghai Municipal Science and Technology Commission Funded Project (16431903300 and 18DZ2291500).

Authors' contributions

WC, YS and XW designed the research. FL developed methods, analyzed data, organized figures, wrote the manuscript, and performed most of the experiments. YL and XW reviewed and revised the manuscript. MW, XX and FZ participated in the animal experiments. All authors read and approved the final manuscript.

Acknowledgements

We would like to express our sincere thanks to Xinqing Fu (Songshan Hospital of Qingdao, China) for the gorgeous drawing of Scheme 1.

References

- [1] Song C, Phuengkham H, Kim YS, Dinh VV, Lee I, Shin IW, et al. Syringeable immunotherapeutic nanogel reshapes tumor microenvironment and prevents tumor metastasis and recurrence. *Nat Commun.* 2019;10:3745.
- [2] Ahmed J, Chard LS, Yuan M, Wang J, Howells A, Li Y, et al. A new oncolytic Vaccinia virus augments antitumor immune responses to prevent tumor recurrence and metastasis after surgery. *Immunother Cancer.* 2020;8:e000415.
- [3] Tohme S, Simmons RL, Tsung A. Surgery for cancer: A trigger for metastases. *Cancer Res.*

2017;77:1548-52.

- [4] Bregni G, Akin Telli T, Camera S, Deleporte A, Moretti L, Bali AM, et al. Adjuvant chemotherapy for rectal cancer: Current evidence and recommendations for clinical practice. *Cancer Treat Rev.* 2020;83:101948.
- [5] Pan XB, Li L, Qu S, Chen L, Liang SX, Zhu XD. The efficacy of chemotherapy in survival of stage II nasopharyngeal carcinoma. *Oral Oncol.* 2020;101:104520.
- [6] Donovan LE, Lassman AB. Chemotherapy treatment and trials in low-grade gliomas. *Neurosurg Clin.* 2019;30:103-9.
- [7] Ongnok B, Chattipakorn N, Chattipakorn SC. Doxorubicin and cisplatin induced cognitive impairment: The possible mechanisms and interventions. *Exp Neurol.* 2020;324:113118.
- [8] Negrette-Guzmán M. Combinations of the antioxidants sulforaphane or curcumin and the conventional antineoplastics cisplatin or doxorubicin as prospects for anticancer chemotherapy. *Eur J Pharmacol.* 2019;859:172513.
- [9] Wang X, Cao W, Zhang J, Yan M, Xu Q. A covalently bound inhibitor triggers EZH2 degradation through CHIP-mediated ubiquitination. *EMBO J.* 2017;36:1243-60.
- [10] Huis In 't Veld RV, Ritsma L, Kleinovink JW, Que I, Ossendorp F, Cruz LJ. Photodynamic cancer therapy enhances accumulation of nanoparticles in tumor-associated myeloid cells. *J Control Release.* 2020;320:19-31.
- [11] Lo PC, Rodríguez-Morgade MS, Pandey RK, Ng DKP, Torres T, Dumoulin F. The unique features and promises of phthalocyanines as advanced photosensitisers for photodynamic therapy of cancer. *Chem Soc Rev.* 2020;49:1041-56.
- [12] Yi JT, Pan QS, Liu C, Hu YL, Chen TT, Chu X. An intelligent nanodevice based on the synergistic effect of telomerase-triggered photodynamic therapy and gene-silencing for precise cancer cell therapy. *Nanoscale* 2020;12:10380-9.
- [13] Kwiatkowski S, Knap B, Przystupski D, Saczko J, Kędzierska E, Knap-Czop K, et al. Photodynamic therapy - mechanisms, photosensitizers and combinations. *Biomed Pharmacother.* 2018;106:1098-107.
- [14] Donohoe C, Senge MO, Arnaut LG, Gomes-da-Silva LC. Cell death in photodynamic therapy: From oxidative stress to anti-tumor immunity. *Biochim Biophys Acta Rev Cancer.* 2019;1872:188308.
- [15] Cheng P, Pu K. Activatable phototheranostic materials for imaging-guided cancer therapy. *ACS Appl Mater Interfaces.* 2020;12:5286-99.
- [16] Wang Y, Xie Y, Li J, Peng ZH, Sheinin Y, Zhou J, et al. Tumor-penetrating nanoparticles for enhanced anticancer activity of combined photodynamic and hypoxia-activated therapy. *ACS Nano.* 2017;11:2227-38.
- [17] He H, Zhu R, Sun W, Cai K, Chen Y, Yin L. Selective cancer treatment via photodynamic sensitization of hypoxia-responsive drug delivery. *Nanoscale.* 2018;10:2856-65.
- [18] Dai Y, Wang B, Sun Z, Cheng J, Zhao H, Wu K, et al. Multifunctional theranostic liposomes loaded with a hypoxia-activated prodrug for cascade-activated tumor selective combination therapy. *ACS Appl Mater Interfaces.* 2019;11:39410-23.
- [19] Boca S, Gulei D, Zimta AA, Onaciu A, Magdo L, Tigu AB, et al. Nanoscale delivery systems for microRNAs in cancer therapy. *Cell Mol Life Sci.* 2019;77:1059-86.
- [20] Ferraris C, Cavalli R, Panciani PP, Battaglia L. Overcoming the blood-brain barrier: successes and

- challenges in developing nanoparticle-mediated drug delivery systems for the treatment of brain tumours. *Int J Nanomedicine*. 2020;15:2999-3022.
- [21] McClements DJ. Advances in nanoparticle and microparticle delivery systems for increasing the dispersibility, stability, and bioactivity of phytochemicals. *Biotechnol Adv*. 2020;38:107287.
- [22] Wang J, Hu X, Xiang D. Nanoparticle drug delivery systems: an excellent carrier for tumor peptide vaccines. *Drug Deliv*. 2018;25:1319-27.
- [23] Lim S, Park J, Shim MK, Um W, Yoon HY, Ryu JH, et al. Recent advances and challenges of repurposing nanoparticle-based drug delivery systems to enhance cancer immunotherapy. *Theranostics*. 2019;9:7906-23.
- [24] Huang P, Wang X, Liang X, Yang J, Zhang C, Kong D, et al. Nano-, micro-, and macroscale drug delivery systems for cancer immunotherapy. *Acta Biomater*. 2019;85:1-26.
- [25] Sun CY, Cao Z, Zhang XJ, Sun R, Yu CS, Yang X. Cascade-amplifying synergistic effects of chemo-photodynamic therapy using ROS-responsive polymeric nanocarriers. *Theranostics*. 2018;8:2939-53.
- [26] Panikar SS, Ramírez-García G, Vallejo-Cardona AA, Banu N, Patrón-Soberano OA, Cialla-May D, et al. Novel anti-HER2 peptide-conjugated theranostic nanoliposomes combining NaYF₄:Yb,Er nanoparticles for NIR-activated bioimaging and chemo-photodynamic therapy against breast cancer. *Nanoscale*. 2019;11:20598-613.
- [27] Yang GG, Hao L, Cao Q, Zhang H, Yang J, Ji LN, et al. Three-in-one self-assembled nanocarrier for dual-drug delivery, two-photon imaging, and chemo-photodynamic synergistic therapy. *ACS Appl Mater Interfaces*. 2018;10:28301-13.
- [28] Wang M, Zhai Y, Ye H, Lv Q, Sun B, Luo C, et al. High co-loading capacity and stimuli-responsive release based on cascade reaction of self-destructive polymer for improved chemo-photodynamic therapy. *ACS Nano*. 2019;13:7010-23.
- [29] Jing X, Zhi Z, Jin L, Wang F, Wu Y, Wang D, et al. pH/redox dual-stimuli-responsive cross-linked polyphosphazene nanoparticles for multimodal imaging-guided chemo-photodynamic therapy. *Nanoscale*. 2019;11:9457-67.
- [30] Huang Y, Xiao Z, Guan Z, Shen Y, Jiang Y, Xu X, et al. A light-triggered self-reinforced nanoagent for targeted chemo-photodynamic therapy of breast cancer bone metastases via ER stress and mitochondria mediated apoptotic pathways. *J Control Release*. 2020;319:119-34.
- [31] Peng H, Qin YT, He XW, Li WY, Zhang YK. Epitope molecularly imprinted polymer nanoparticles for chemo-/photodynamic synergistic cancer therapy guided by targeted fluorescence imaging. *ACS Appl Mater Interfaces*. 2020;12:13360-70.
- [32] Zhang Z, Wang R, Huang X, Luo R, Xue J, Gao J, et al. Self-delivered and self-monitored chemo-photodynamic nanoparticles with light-triggered synergistic antitumor therapies by downregulation of HIF-1 α and depletion of GSH. *ACS Appl Mater Interfaces*. 2020;12:5680-94.
- [33] Suk JS, Xu Q, Kim N, Hanes J, Ensign LM. PEGylation as a strategy for improving nanoparticle-based drug and gene delivery. *Adv Drug Deliv Rev*. 2016;99:28-51.

Figures

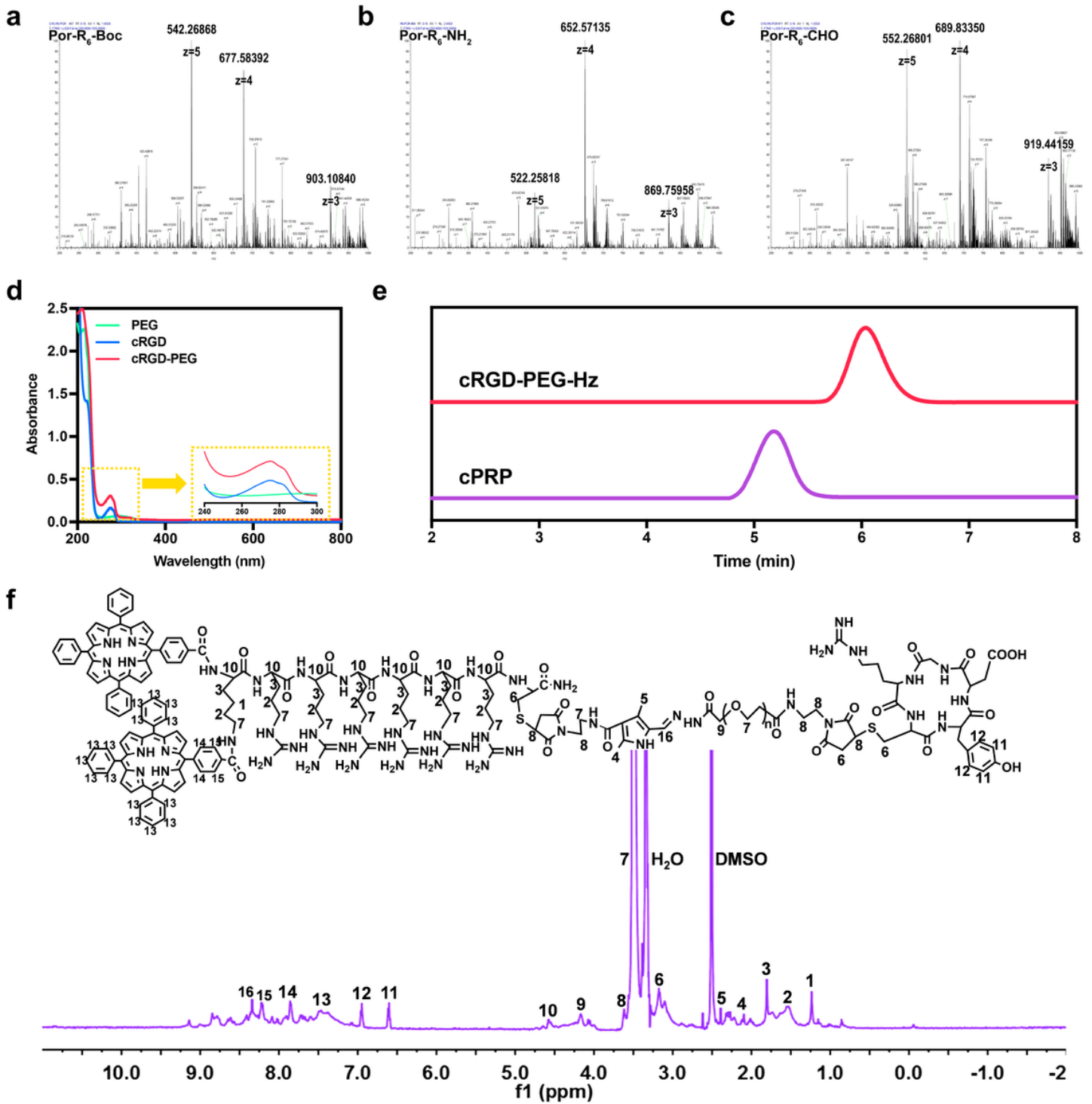


Figure 1

Mass spectrum of (a) Por-R₆-Boc, (b) Por-R₆-NH₂, and (c) Por-R₆-CHO. (d) UV-vis spectrum of cRGD-PEG, PEG and cRGD. (e) GPC spectra of cPRP and cRGD-PEG. (f) ¹H-NMR spectra of cPRP.

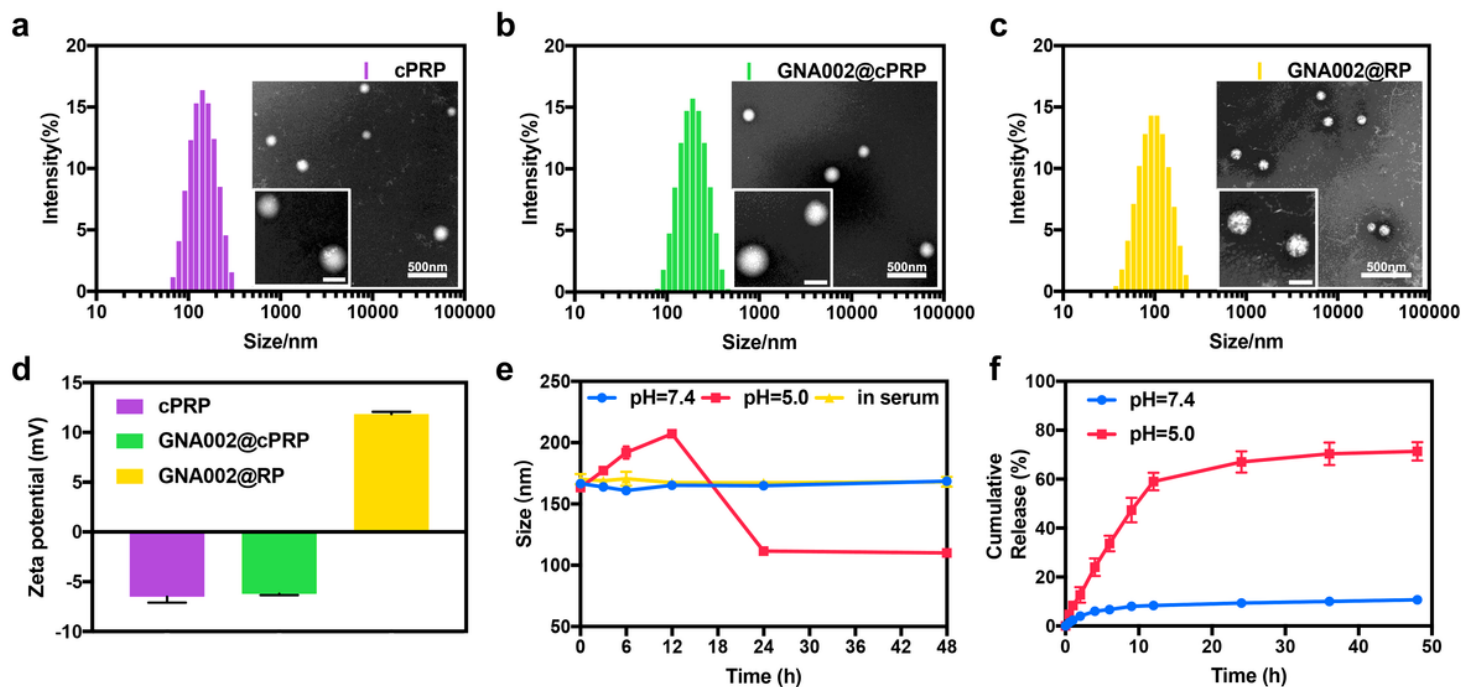


Figure 2

(a) The size (DLS) and TEM of blank cPRP, (b) GNA002@cPRP, and (c) GNA002@RP nanoparticles. Scale bar: 500 nm (100 nm inset). (d) Zeta potentials of blank cPRP, GNA002@cPRP, and GNA002@RP nanoparticles. (e) Size changes of GNA002@cPRP in PBS (pH 7.4 and 5.0) and serum over 48 h. (f) The release profiles of GNA002@cPRP nanoparticles in PBS (pH 7.4 and 5.0) with 0.1% Tween 80 at 37°C.

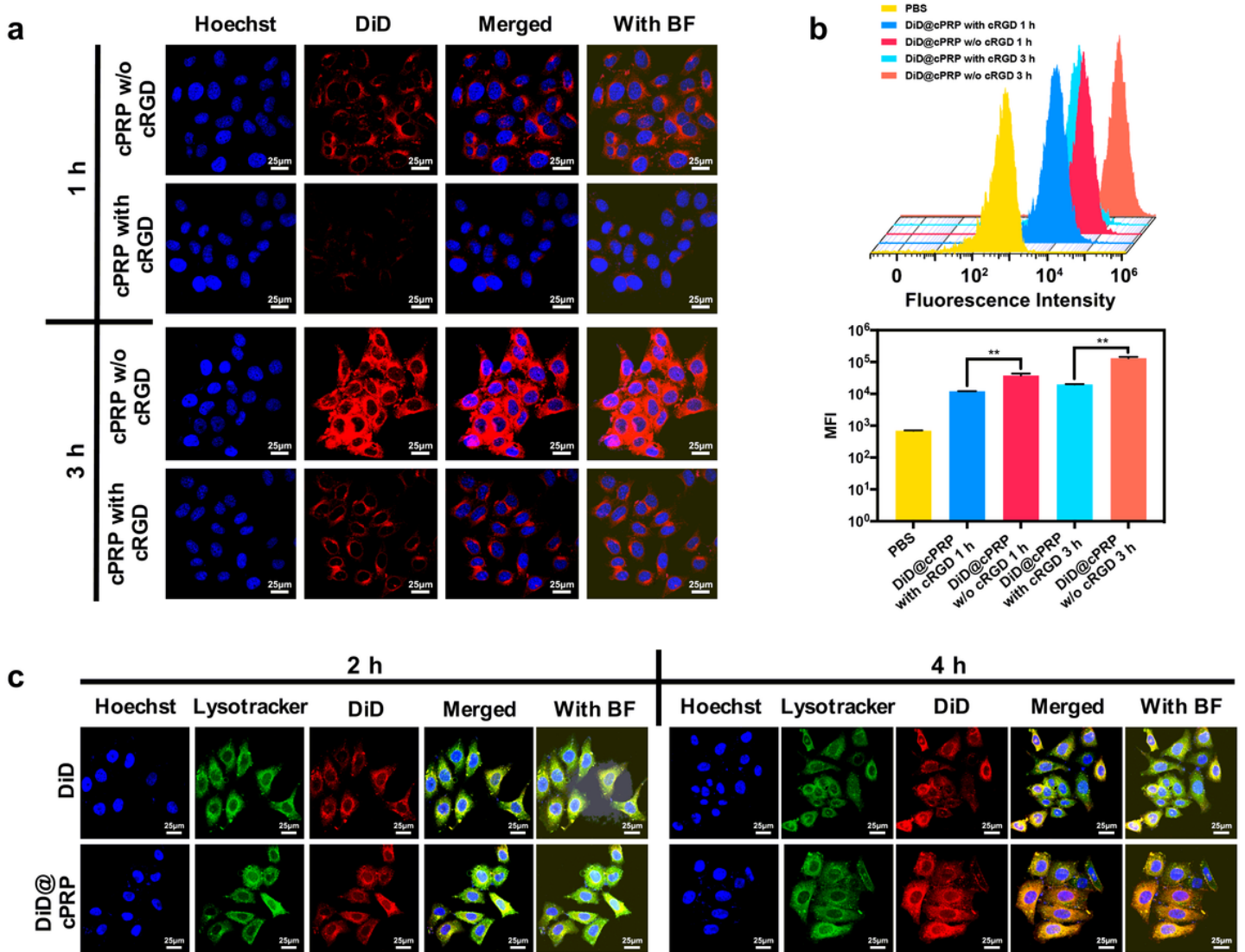


Figure 3

Cellular uptake of HeLa cells after 1 h and 3 h incubation with DiD@cPRP nanoparticles monitored by (a) CLSM, (b) flow cytometry profiles and mean fluorescence intensity. The red fluorescence indicates DiD@cPRP nanoparticles and the blue fluorescence indicates the cell nuclei. (c) DiD delivery tracking in HeLa cells after 2 h and 4 h incubation with free DiD and DiD@cPRP nanoparticles detected by CLSM. The blue, red and green fluorescence indicate cell nuclei, lysosomes and DiD as well as DiD@cPRP nanoparticles, respectively. Scale bar: 25 μ m. Data are shown as mean \pm SD (n = 3) (**P < 0.01).

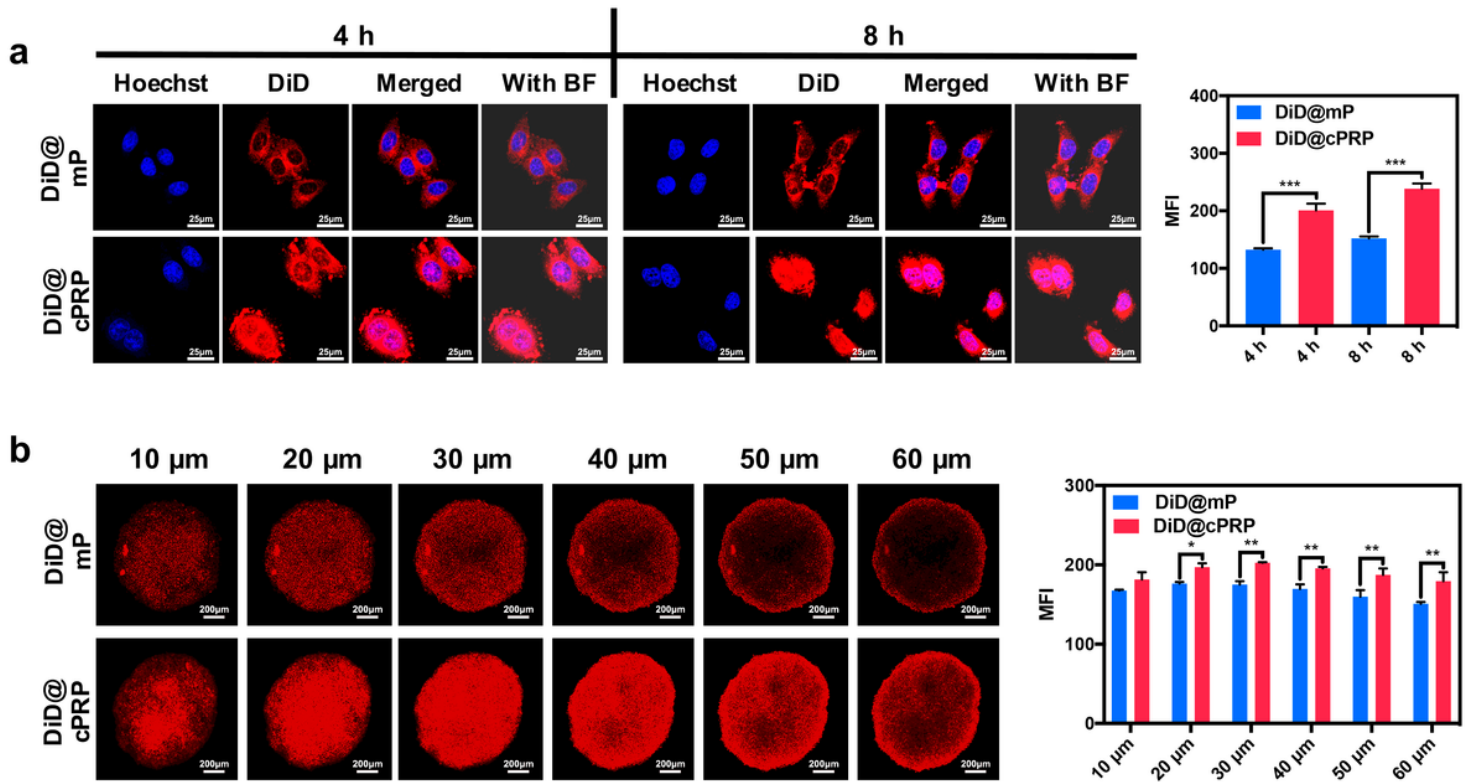


Figure 4

(a) DiD nuclei distribution in HeLa cells after 4 h and 8 h incubation with DiD@mP and DiD@cPRP nanoparticles monitored by CLSM and mean fluorescence intensity. Scale bar: 25 μ m. (b) DiD penetration in HeLa MCSs after 4 h incubation with DiD@mP and DiD@cPRP nanoparticles monitored by CLSM and mean fluorescence intensity. Scale bar: 200 μ m. Data are shown as mean \pm SD ($n = 3$) (* $P < 0.05$, ** $P < 0.01$ and *** $P < 0.001$).

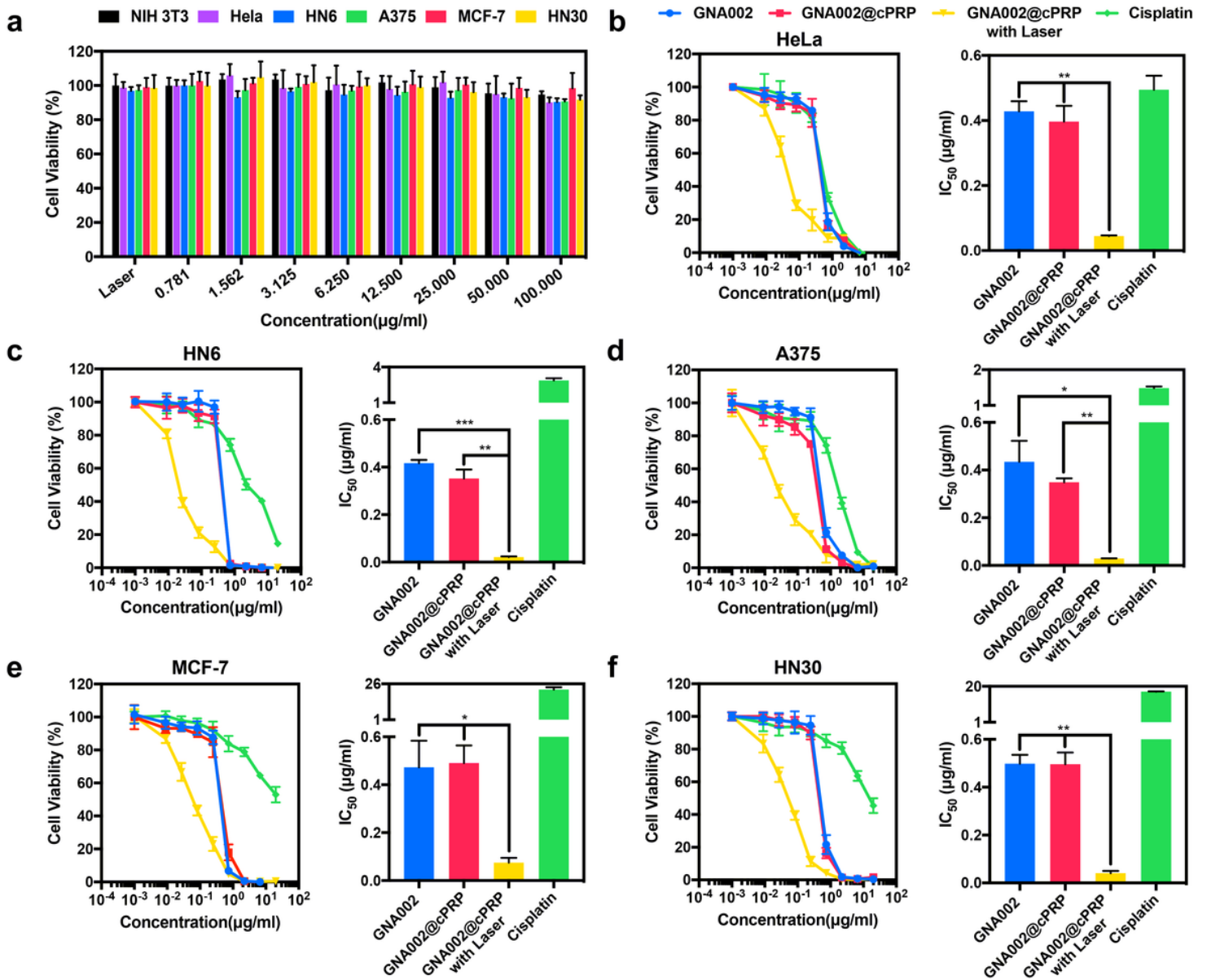


Figure 5

(a) Cytotoxicity of blank cPRP nanoparticles and laser irradiation in NIH 3T3, HeLa, HN6, A375, MCF-7, and HN30 cells measured by CCK-8 assay. Viability and IC₅₀ of (b) HeLa, (c) HN6, (d) A375, (e) MCF-7, and (f) HN30 cells after 48 h incubation with different treatments. Data are shown as mean ± SD (n=3) (*P < 0.05, **P < 0.01 and ***P < 0.001).

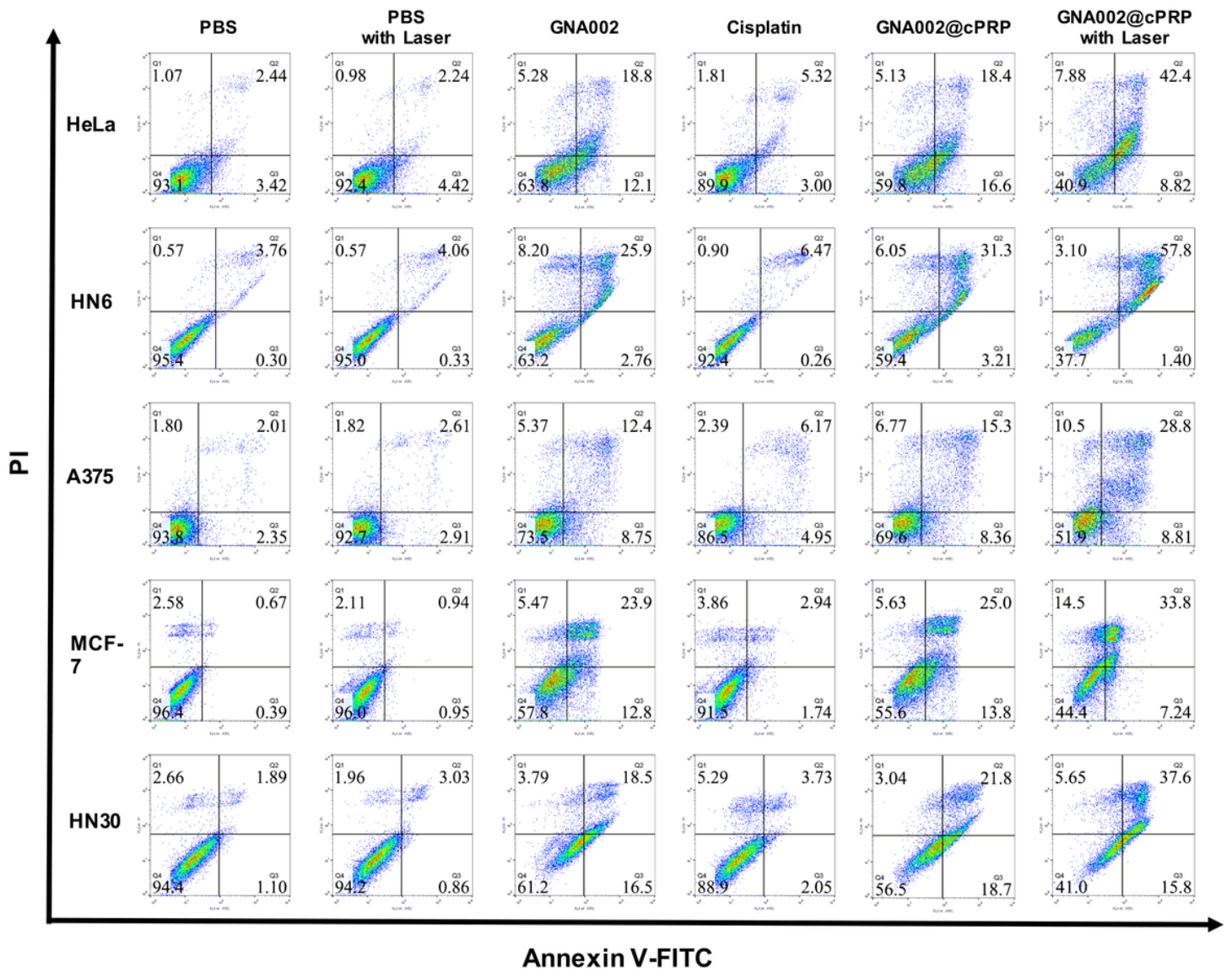


Figure 6

Apoptosis assessment of HeLa, HN6, A375, MCF-7, and HN30 cells after 48 h incubation with different treatments.

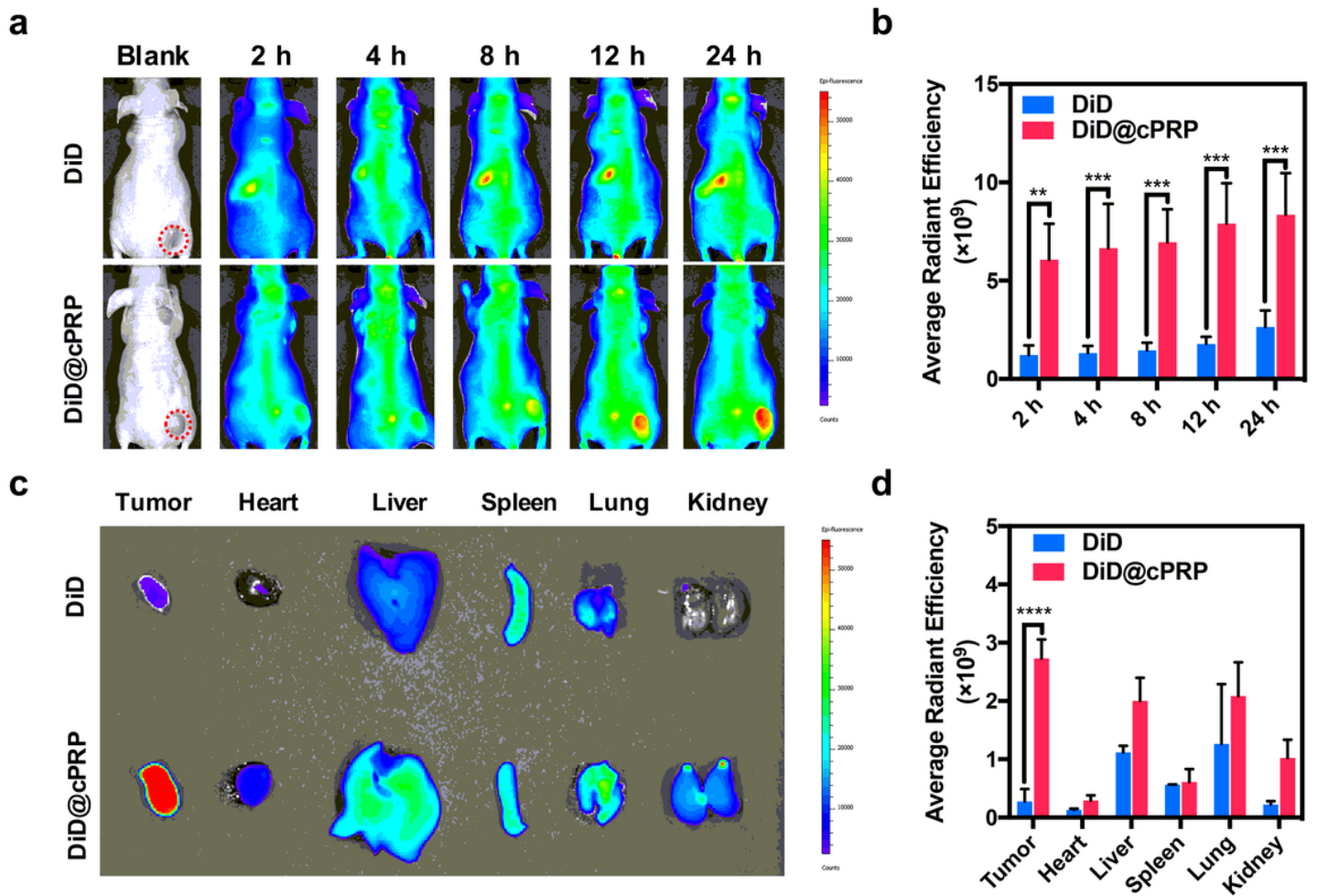


Figure 7

(a) In vivo images of HeLa cancer-bearing mice at prescribed time and (b) real-time average radiant efficiency of tumor sites after tail vein injection of DiD and DiD@cPRP nanoparticles. (c) Ex vivo images and (d) average radiant efficiency of tumors and major organs after 24 h tail vein injection. Data are shown as mean \pm SD ($n = 3$) (** $P < 0.01$, *** $P < 0.001$ and **** $P < 0.0001$).

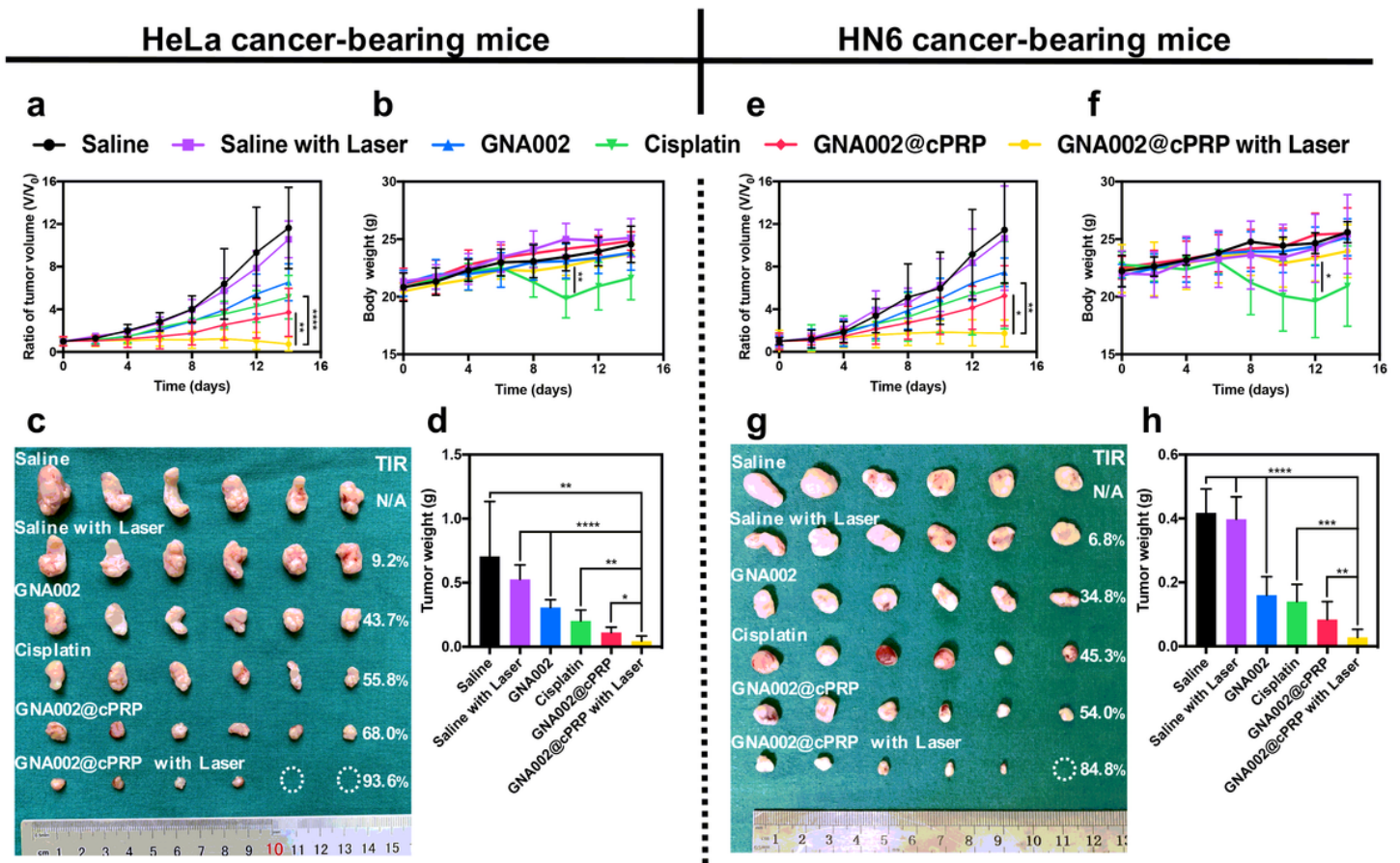


Figure 8

HeLa cancer-bearing mice: (a) Tumor growth curves and (b) body weight changes of different treatment groups over the treatment period. (c) Photographs as well as tumor inhibition ratio (TIR) values and (d) tumor weights of different treatment groups after sacrifice. HN6 cancer-bearing mice: (e) Tumor growth curves and (f) body weight changes of different treatment groups over the treatment period. (g) Photographs as well as tumor inhibition ratio (TIR) values and (h) tumor weights of different treatment groups after sacrifice. Data are shown as mean \pm SD ($n = 6$). (* $P < 0.05$, ** $P < 0.01$, *** $P < 0.001$ and **** $P < 0.0001$).

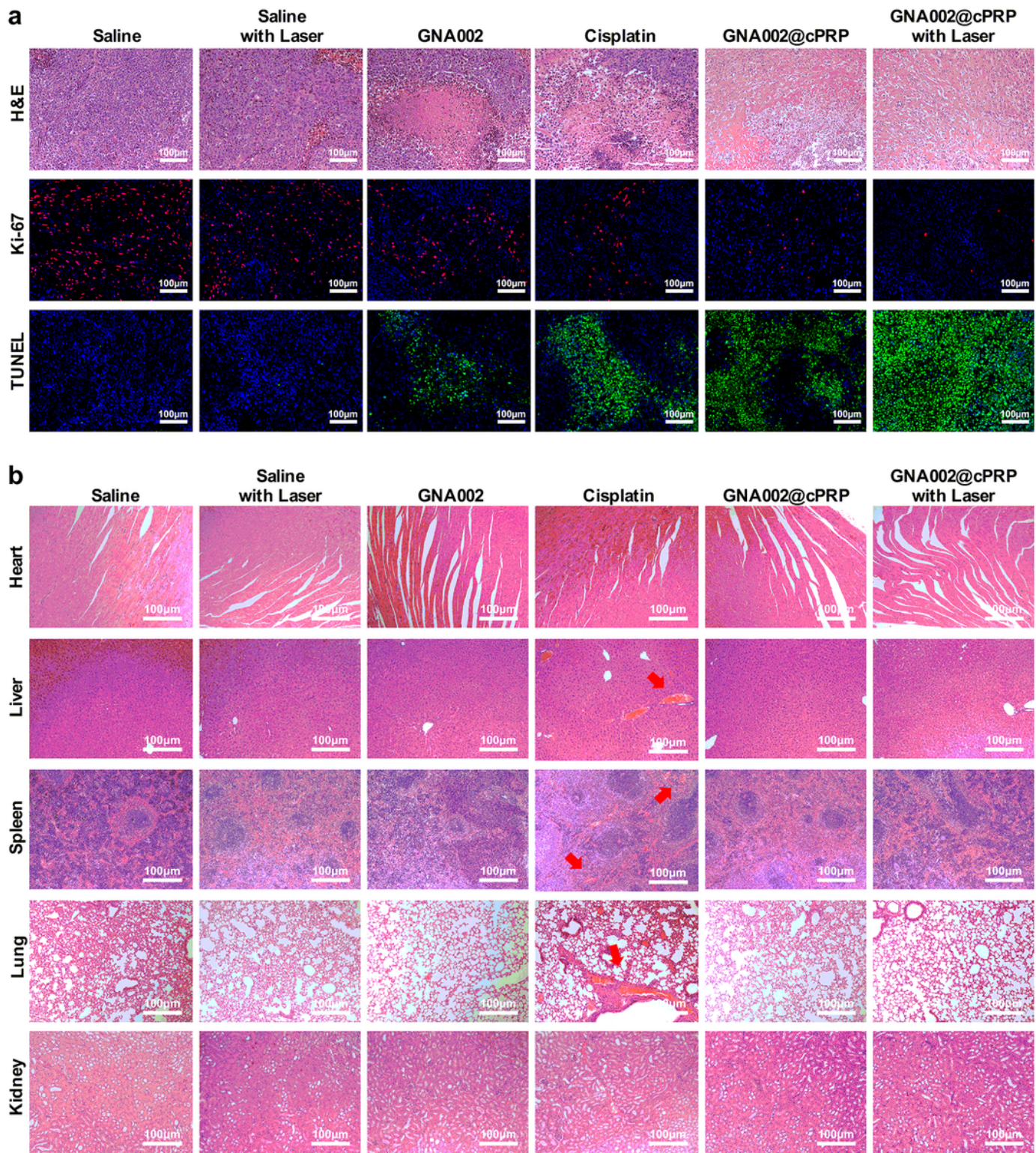


Figure 9

(a) Histological analyses of tumor sections of HeLa cancer-bearing mice following treatments with H&E, TUNEL and Ki-67 staining. (b) Histological assessment of the major organs of HeLa cancer-bearing mice following treatments with H&E staining. Scale bar: 100 μ m.

Supplementary Files

This is a list of supplementary files associated with this preprint. Click to download.

- [Scheme1.tif](#)
- [Supplementarymaterial.docx](#)